3 **Scalable fabrication of > 90 cm² perovskite solar modules with > 1000**
4 **h operational stability based on the intermediate phase strategy**

5 *Guoqing Tong, Dae-Yong Son, Luis K. Ono, Yuqiang Liu, Yanqiang Hu, Hui Zhang,*
6 *Afshan Jamshaid, Longbin Qiu, Zonghao Liu, and Yabing Qi*[*]
7 Dr. G. Tong, Dr. D.-Y. Son, Dr. L. K. Ono, Dr. Y. Liu, Mr. Y. Hu, Dr. H. Zhang, Ms.
8 A. Jamshaid, Dr. L. Qiu, Dr. Z. Liu, Prof. Y. B. Qi
9 Energy Materials and Surface Sciences Unit (EMSSU)
10 Okinawa Institute of Science and Technology Graduate University (OIST)
11 1919-1 Tancha, Onna-son, Kunigami-gun, Okinawa 904-0495, Japan
12 *Corresponding author: Yabing Qi, E-mail: Yabing.Qi@OIST.jp

13

14 **Abstract:** In addition to high efficiencies, upscaling and long-term operational stability
15 are key pre-requisites for moving perovskite solar cells towards commercial
16 applications. In this work, we develop a strategy to fabricate large-area uniform and
17 dense perovskite films with a thickness over one-micrometer via a two-step coating
18 process by introducing NH_4Cl as an additive in the PbI_2 precursor solution.
19 Incorporation of NH_4Cl induces the formation of the intermediate phases of
20 $x[NH_4^+] \cdot [PbI_2Cl_x]^{x-}$ and $HPbI_{3-x}Cl_x$, which can effectively retard the crystallization rate
21 of perovskite leading to uniform and compact full-coverage perovskite layers across
22 large areas with high crystallinity, large grain sizes, and small surface roughness. Our
23 5×5 cm² and 10×10 cm² perovskite solar modules (PSMs) based on this method
24 achieved a power conversion efficiency (PCE) of 14.55% and 10.25%, respectively.
25 These PSMs also exhibited good operational stability with a T_{80} (the time during which
26 the solar module PCE drops to 80% of its initial value) lifetime under continuous light
27 illumination exceeding 1600 h (5×5 cm²) and 1100 h (10×10 cm²), respectively.

28

29 **1. Introduction**

30   Outstanding efficiencies in lab-scale perovskite solar cells (PSCs), with the certified
31 power conversion efficiency (PCE) of 25.5% (~ 0.1 cm²) and 21.6% (~1 cm²), have
32 been achieved by employing multiple techniques during the past decade of research.[1-
33 4] Although the high PCEs achieved on lab-scale PSCs are now comparable with the

commercial silicon and copper indium gallium selenide (CIGS) solar cells, the performance (i.e., efficiency and stability) of perovskite solar modules (PSMs) are still far inferior to the commercial photovoltaics. For example, the PCE of PSMs is around 19% with an active area over 10 cm^2, which is much smaller than ~10000 cm^2 achieved in CIGS solar cells.[5-8] In addition, degradation of solar cell performance during operation is another key issue impeding the deployment of PSMs in practical applications. A survey of operational stability profiles based on previous reports indicates that modules size of reported PSMs are typically smaller than 50 cm^2 and the lifetime mostly shorter than 1000 h (Table S1 and Figure S1, Supporting Information).[5, 9-11] Therefore, fabrication of large scale PSMs with high efficiency and long-term operational stability is currently still a significant challenging.

The large decrease in efficiency of PSCs when upscaling from small lab-scale cells to larger-size modules is a result of the following factors:[4-5, 7, 12] (1) the poor interfacial contact between perovskite and electron transport layer (ETL)/hole transport layer (HTL); (2) amplified effects of morphological imperfections in the perovskite layer (e.g., defects, voids/pinholes, impurities) in large areas resulting in enhanced carrier recombination events in PSMs; (3) series resistance related issues when scaling up the transparent conductive oxides; (4) increased fabrication complexity related to creation of sub-cells and interconnections between them. Points (1) and (2) mentioned above have an immense impact on the PCEs of PSMs, and are the main focus of this work. It has been reported that the un-controllable kinetics during the transformation from PbI$_2$ to perovskite is the key step that leads to high generation of macroscopic voids/pinholes. In addition, it also leads to microscopic defects/traps within perovskite grains and at grain boundaries (GBs), which lead to increased carrier recombination and carrier diffusion length often below 1 μm.[13] This is the reason why high efficiency PSCs are based on thin layers of perovskites with a thickness below one-micrometer. On the other hand, several recent studies found that thick perovskite films with a long carrier diffusion length and a low defect density can achieve PCE comparable with thin film PSCs (Table S2, Supporting information).[12, 14] For example, inkjet-printed PSCs employing the 1.5 μm triple-cation perovskite film were reported by Eggers and

coworkers, which showed an efficiency over 21% with an area of 0.105 cm^2 and stabilized power output PCE of 18.5%.[15] Furthermore, the work by Chen and coworkers reported that the thick perovskite films (0.7 – 1.15 μm) also helped prevent penetration of moisture inside the perovskite layer, which effectively retarded degradation of PSCs.[16] Previously, Qi and coworkers reported high quality perovskite films with a thickness over one-micrometer enabling fabrication of 5 × 5 cm^2 PSMs with high reproducibility and an active area PCE of 15.3% (active area = 12 cm^2; geometric fill factor (GFF) = 48%).[12] Therefore, employment of thick uniform perovskite films is a promising strategy to deposit perovskite films with a full coverage on large area substrates, which helps minimize voids/pinholes and improve the PCE, stability, reproducibility and device yield.

However, the fast and uncontrollable crystallization process of the conventional solution-based approach often induces the formation of polycrystalline films with small grain sizes and a large number of GBs. This situation is further aggravated when considering fabrication of thick perovskite films in large-area PSMs, especially with areas over 10 × 10 cm^2. The fast and uncontrollable nucleation rate during perovskite formation increases the chances of large variations in stoichiometry and film thickness, and leads to many macroscopic voids/pinholes across large areas.[12] In addition, the low solubility of PbI$_2$ compared to the methylammonium iodide (MAI) and formamidinium iodide (FAI) usually induces the inhomogeneous crystal growth of perovskite in the precursor solution,[17] which aggravates the inhomogeneity of the perovskite layer. Despite the several strategies such as introduction of Lewis based additives, supramolecular materials into PbI$_2$ and/or perovskites to improve the solubility of PbI$_2$ and retard the crystal growth of perovskites, the residue additives and insulating components in the perovskite films also affect carrier transport and operational stability.[17-19]

Recently, the intermediate phase has been proposed to alleviate the fast reaction, which can slow down the nucleation rate and crystal growth of perovskites to enable the complete reaction and lead to high crystallinity.[20-22] For example, Kang, Zhang and coworkers introduced the intermediate phase of NH$_4$PbI$_3$ formed by NH$_4^+$ diffusion to

the $[PbI_6]^{4-}$ octahedral layer, which served as extra heterogeneous nucleation sites to slow down the crystal growth.[20] In addition, Zhao and coworkers introduced an intermediate phase of $HPbI_3$ to replace lead halide precursor in order to fabricate the highly crystalline $FAPbI_3$ perovskite because the exchange of the H^+ ions in the PbI_6 octahedral framework with the FA^+ cations is slower than the reaction rate between PbI_2 and FAI.[23]

Here, we deposit thick perovskite films combining the high solubility and intermediate phase induced growth to fabricate high quality perovskite solar cells and modules. The ammonium chloride (NH_4Cl) is first added into the PbI_2 precursor solution to increase the solubility and concentration of PbI_2 in DMF. The resultant thick perovskite absorber layer prepared by high concentration PbI_2 precursor solution can increase the tolerance for the thickness fluctuation and reduce the risk of forming voids and pinholes in the large scale. In addition, the formation of the two intermediate phases of $x[NH_4^+]\bullet[PbI_2Cl_x]^{x-}$ and $HPbI_{3-x}Cl_x$ can effectively retard the nucleation and crystal growth rate of perovskite ~~slow down the crystal growth~~, which benefits the phase transformation from PbI_2 to perovskite (perovskite prepared by the NH_4Cl method is abbreviated as NH_4Cl-perovskite) and improves the quality of the perovskite film. The release of NH_3 ensures no extra residues in the final perovskite films and lowers the stress concentration at GBs in terms of the volume expansion. Based on our strategy, NH_4Cl-assisted two-step spin-coating method was used to fabricated PSCs and PSMs for the first time. The resultant thicker layer PSCs reached a champion PCE of 20.17% in lab-scale sizes (0.09 cm^2) and a high PCE of 14.55% for 5×5 cm^2 PSMs (average PCE of $13.23 \pm 0.63\%$) with a designated area of 22.4 cm^2 (the active area PCE was 16.35 %, GFF = 89%). The excellent upscalability of this strategy is evident when these results are compared with the conventional solution processed modules that resulted in an average PCE of $10.05 \pm 1.58\%$ (active area PCE = 14.84 %; GFF = 88%). Furthermore, a champion PCE of 10.25% for 10×10 cm^2 was achieved by NH_4Cl method with a designated area of 91.8 cm^2 (active area PCE of 12.14%, GFF = 84.4%). Besides, the 5×5 cm^2 and 10×10 cm^2 PSMs exhibited excellent operational stability with T_{80} lifetimes exceeding 1625 h and 1157 h, respectively, under continuous

1 operation conditions in dry N_2 environment. It is worth noting that this is the first report

2 of the PSM with a designated area over 90 cm^2 showing operational stability exceeding

3 1000 h. As a demonstration, we show a mini-fan and plastic toy car powered by our

4 PSMs in outdoor environment.

5
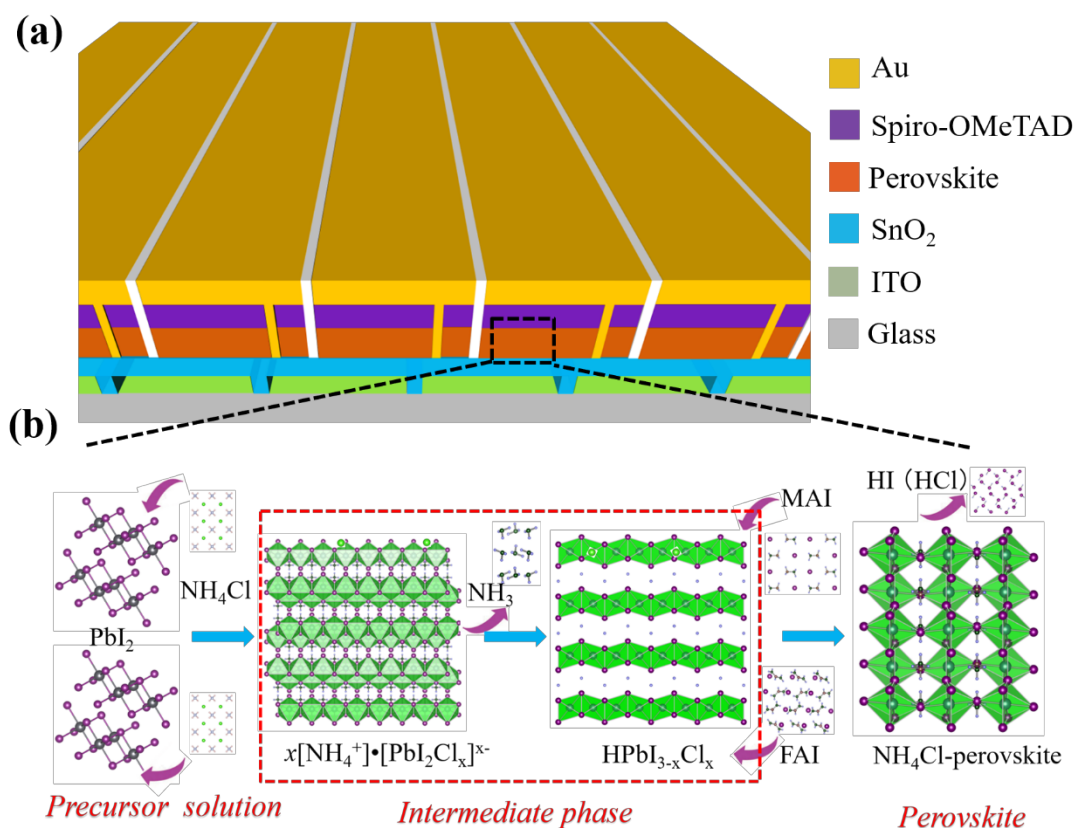
6

7 **Figure 1.** a) Illustration of PSM architecture with substrate areas of 5×5 cm^2 and $10 \times$

8 10 cm^2. b) Summary of the formation process of the NH_4Cl-based perovskite films

9 starting from NH_4Cl and PbI_2 precursors leading to the intermediate phases of

10 $x[NH_4^+] \cdot [PbI_2Cl_x]^{x-}$ and $HPbI_{3-x}Cl_x$. The composition of perovskite is

11 $Cs_{0.05}FA_{0.54}MA_{0.41}Pb(I_{0.98}Br_{0.02})_3$.

12

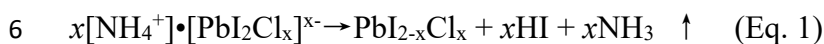13 **2. Results and Discussion**

14 **2.1. Fabrication of thick perovskite films with intermediate phase engineering.**

15 The standard two-step coated thin perovskite films (300-500 nm) are fabricated by

16 spin-coating a 1 M PbI_2/DMF solution or by thermally evaporating 180 - 200 nm PbI_2

17 films followed by the coating of an organic cation-precursor solution.[24-26] To prepare

thick perovskite films, it is necessary to use a high concentration of PbI_2 solution

because the formation of final perovskite layer is proportional to the PbI_2 precursor

layer thickness. In this work, we chose a concentration of 2.2 M PbI_2/DMF to achieve

fabrication of thick perovskite films. Unfortunately, the PbI_6 octahedral colloids are

prone to precipitate in the organic solvent with the formation of PbI_2-DMF-contained

solvate phases,[27-28] which limits the solubility of PbI_2 in the DMF solution (~1.0 M)

and makes it difficult to realize a precursor solution with high PbI_2 concentration.[27-28]

Inspired by the report that NH^{4+} can form hydrogen bonds with I-Pb-I to form an

intermediate phase with improved solubility of PbI_2 and perovskites,[29-30] we added 0-

1 M NH_4Cl into the 1 M and 2.2 M PbI_2/DMF solution as additive, respectively, and

studied the solubility of PbI_2 in DMF with the addition of NH_4Cl. We found that 1 M

PbI_2 can be readily dissolved in DMF with different amounts of NH_4Cl at room

temperature after shaking the solution for 2 min (Figure S2, Supporting Information)

because of the formation of the intermediate phase of $x[NH_4^+] \cdot [PbI_2Cl_x]^{x-}$. But the 2.2

M PbI_2 in DMF did not dissolve completely at room temperature after shaking the

solution for 2 min (Figure S3, Supporting Information). On the other hand, when we

heated the solution to 70 ºC and stirred it for 10 minutes with the NH_4Cl molar ratio

over 0.4 M (Figures S4, S5, Supporting Information), the 2.2 M PbI_2 was completely

dissolved. This can be explained by the fact that the NH_4^+ cations diffuse into PbI_2 to

construct an intermediate phase of $x[NH_4^+] \cdot [PbI_2Cl_x]^{x-}$,[30] which can significantly

promote the dissolution of PbI_2 in the DMF solvent.[20, 30]

To investigate the intermediate phase, we carried out XRD and SEM measurements.

It is found that upon increasing the NH_4Cl content to 0.4 M, the grain size and

crystallinity of the PbI_2 film also increase (Figures S6, S7, Supporting Information).

Contrary to our expectations, in our XRD results, the peak corresponding to

$x[NH_4^+] \cdot [PbI_2Cl_x]^{x-}$ at around 9.4º was not observed.[20] Instead, another peak at 11.5º

was detected, which is assigned to the $HPbI_{3-x}Cl_x$ phase.[31] The above results suggest

that the $x[NH_4^+] \cdot [PbI_2Cl_x]^{x-}$ intermediate phase is highly unstable and transforms

immediately to the $HPbI_{3-x}Cl_x$ phase in the films. An additional XRD measurement with

different measurement conditions was performed to confirm the above observation.

When NH_4Cl-PbI_2 films were prepared by drop-casting and XRD was immediately measured, a small XRD peak at 9.4^o was detected (Figure S8, Supporting Information). This result corroborates the fast conversion from $x[NH_4^+] \cdot [PbI_2Cl_x]^{x-}$ to $HPbI_{3-x}Cl_x$ possibly due to the phase transformation as follows:[12, 31-32]

$$x[NH_4^+] \cdot [PbI_2Cl_x]^{x-} \rightarrow PbI_{2-x}Cl_x + xHI + xNH_3 \uparrow \quad \text{(Eq. 1)}$$
$$PbI_{2-x}Cl_x + HI \rightarrow HPbI_{3-x}Cl_x \quad \text{(Eq. 2)}$$

To confirm this hypothesis, we performed Fourier transform infrared spectroscopy (FTIR) and mass spectrometry (MS) measurements on the NH_4Cl-PbI_2 and pure-PbI_2 films. An increased FTIR peak corresponding to the N-H stretching vibration mode in the NH_4Cl-PbI_2 film in comparison to the pure PbI_2 film (Figure S9, Supporting Information) implies the formation of the intermediate phase of $x[NH_4^+] \cdot [PbI_2Cl_x]^{x-}$.[20, 33] MS experiments were performed to verify whether NH_3 is released from the intermediate phase film as described by eq. 1. As shown in Figure S10 (Supporting Information), when the NH_4Cl-PbI_2 film is inserted in the MS vacuum chamber, a large NH_3 signal (m/z=17 amu) is detected. In addition, the heating experiment results from the MS measurements also corroborate (Figure S10, Supporting Information) the significant release of NH_3, which is consistent with Eq. 1. The presence of intermediate phases can slow down the nucleation rate of perovskite crystals and the effect of chlorine on perovskite film growth as follows:[20, 29, 31-32]

$$HPbI_{3-x}Cl_x + MAI/FAI \rightarrow MA/FAPbI_3 + HI \uparrow + HCl \uparrow \quad \text{(Eq. 3)}$$

The increased peak intensity at 14°, the improvements of the grain size, enhanced light absorption (Figure S11-S14, Supporting Information) and crystallinity of perovskite films with ideal amount (0.4 M) of NH_4Cl after spin-coating the cation solution of FAI/MAI are ascribed to the presence of intermediate phases of $x[NH_4^+] \cdot [PbI_2Cl_x]^{x-}$ in the solution and $HPbI_{3-x}Cl_x$ in the films as illustrated in **Figure 1**. The volatile NH_3 and HI (HCl) byproducts imply no extra residues from $HPbI_{3-x}Cl_x$ remain in the films after the annealing process. This volatilization process can also effectively facilitate the phase transformation process from top to bottom and reduce

the stress at the GBs.[34] This issue was discussed in a previous study[35] and was associated with the low reproducibility of PSCs.
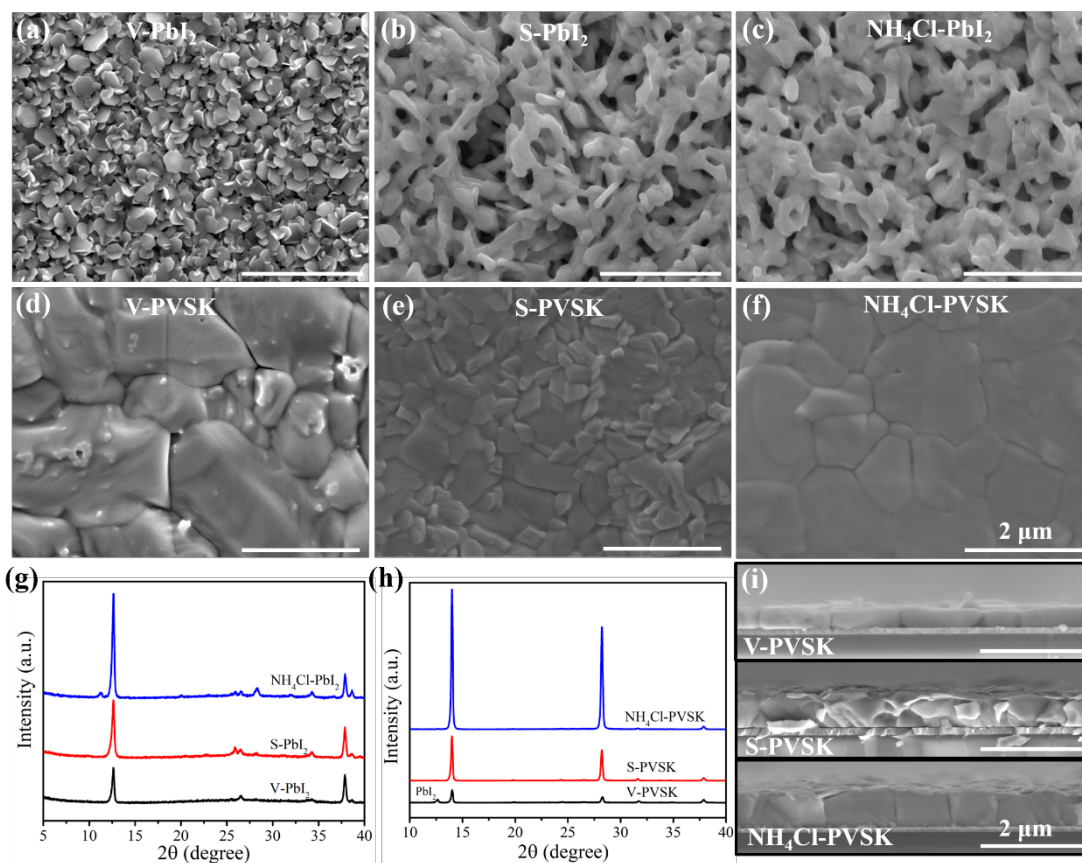
Figure 2. Top-view scanning electron microscopy (SEM) images of a) vapor deposited PbI$_2$ (V-PbI$_2$), b) solution processed PbI$_2$ (S-PbI$_2$) as the control films, c) and the solution processed NH$_4$Cl-PbI$_2$ film. The corresponding SEM images of perovskite films are shown in d) V-PVSK, e) S-PVSK and f) NH$_4$Cl-PVSK. X-ray diffraction (XRD) patterns of g) PbI$_2$ films and h) perovskite films prepared by different methods. i) Cross-section SEM images of the perovskite films.

It is found that 2.2 M PbI$_2$ can be used to prepare the thick PbI$_2$ precursor layer to enable the final perovskite layer with a thickness of one-micrometer (Figure S13, Supporting Information). To make a comparison, an additional control sample consisting of 400 nm PbI$_2$ was deposited on the ITO substrates by the conventional vapor deposition method (V-PbI$_2$). The volume expansion from the intercalation of MAI or FAI results in a volume increase of 2~3 times accompanying the transformation

from PbI_2 to the perovskite.[24-25, 36] As we can see in **Figure 2**a, the V-PbI_2 sample shows a stacking of two-dimensional layered nanosheet structure with grain sizes of 200–300 nm. Different from the evaporated PbI_2 film, the conventional solution processed PbI_2 films without NH_4Cl (S-PbI_2) and with 0.4 M NH_4Cl (NH_4Cl-PbI_2) showed the sponge-like porous surface structure. In addition, the strong XRD peak of NH_4Cl-PbI_2 at 12.6° (Figure 2g) indicates that the use of NH_4Cl can significantly improve the crystallinity of PbI_2. After the spin-coating of MA/FA cation solution and post-annealing, the obtained perovskite film as seen in Figures 2d-2f is a full-coverage compact layer. It is found that surface morphology of conventional solution processed perovskite shows small grain sizes around 200-300 nm, and uneven grain size distribution in the vapor-based perovskite film. In contrast, the NH_4Cl-perovskite film exhibits high crystallinity and large grain size over one-micrometer with uniform distribution (Figures 2f and 2i). Additionally, in comparison to the control solution perovskite and NH_4Cl-perovskite film, the low crystallinity of perovskite film in the case of vapor deposition is observed due to the fact that the dense and thicker PbI_2 film hinders the permeation of cation solution from top to bottom layer,[37] which causes an uneven reaction and inferior light absorption (Figure S15a, Supporting Information). A strong peak at 12.6 °C (Figure 2h) is presumably related to the unreacted PbI_2 in the final vapor deposition processed perovskite layer. In contrast, the porous PbI_2 nature produced by the solution technique can facilitate the penetration of MA/FA cation solution. The complete transformation from PbI_2 to perovskite produces one-micrometer thickness of perovskite films for the conventional solution process and NH_4Cl-based method. Note that the small grain sizes of perovskite crystals and uneven distribution in the cross section of the solution processed perovskite film. As comparison, the NH_4Cl-perovskite film shows the monolithic structure for the crystal grains from the bottom to top with large grain size (1-2 μm) and uniform distribution in Figure 2i. Additionally, a high quality of the perovskite layers and proper interface contacts between the perovskite layer and ETL/HTL help achieve high performance solar cells.[7, 38] The electronic structures of perovskite films were investigated by ultraviolet photoelectron spectroscopy (UPS). As seen in **Figures 3**a-3b, the ionization

energy (IE) values of samples can be extracted by the formula of IE = 21.22 - E_{cutoff} +

E_{onset}[39] and the corresponding values are 5.24 eV (vapor based perovskite), 5.59 eV

(conventional solution processed perovskite) and 5.22 eV (NH$_4$Cl-perovskite),

respectively. Combining with the optical bandgap values extracted from the absorption

spectra (Figure S15b, Supporting Information), we can deduce the electron affinity (EA)

values of these samples (Figure 3c). It is found that the valence band edge of NH$_4$Cl-

PVK shifts upward by about 0.37 eV with respect to the conventional solution

processed perovskite film. ~~because of the presence of Pb^0 and uncoordinated Pb^{2+} in~~

~~the S-PVSK film (Figure S16 and Table S2, Supporting Information). The loss of I$^-$ at~~

~~the surface (MAI/FAI deficient) would increase the IE.~~ To further understand this

valance band edge shift, we performed X-ray photoelectron spectroscopy (XPS)

measurements on the V-PVSK film, the S-PVSK film, and the NH$_4$Cl-PVSK film to

study the film composition and oxidation states of the various elements. It has been

reported that there are two kinds of lead defects in the perovskite film.[40-41] One is

uncoordinated Pb^{2+}, which is usually generated during thermal annealing due to the loss

of volatile organic components.[40] Another kind of defect is metallic lead (Pb^0), which

is often observed during the film fabrication process or solar cell operation.[40] In this

work, we observed the small peaks at 141.67 eV and 136.77 eV in the XPS Pb *4f* region

(Figure S16) corresponding to the metallic Pb (i.e., Pb^0) in the S-PVSK film. In addition,

the Pb^0 peak disappears in the case of the NH$_4$Cl-PVSK film, which indicates that

incorporation of NH$_4$Cl leads to a passivation effect on the perovskite film. Furthermore,

compared to the S-PVSK film, the two spin-orbit splitting peaks of Pb *4f* in the NH$_4$Cl-

PVSK film shift from 143.38 eV and 138.53 eV to lower binding energies of 143.24 eV

and 138.39 eV, which indicates passivation of uncoordinated Pb^{2+}.[40-41] These defects

(Pb^0 and uncoordinated Pb^{2+}) influence the chemical stoichiometry of the perovskite

films, which affects the electronic properties such as IE.[42] MAI deficient (i.e., PbI$_2$

excess) films exhibits a larger IE, while PbI$_2$ deficient (i.e., MAI excess) films show a

smaller IE.[42] In the S-PVSK film, uncoordinated Pb^{2+} resulted from the loss of the

organic components in the fabrication and annealing indicates that the S-PVSK film is

MAI deficient, which leads to a larger IE. In contrast, the NH$_4$Cl-PVSK has a I/Pb atom

ratio of 3.14 (based on our XPS data in Table S3), which means that the NH4Cl-PVSK is slightly MAI rich at the surface and therefore has a smaller IE than S-PVSK.[42] Therefore, an improved energy level alignment at the interface between the NH4Cl-PVSK and HTL can reduce energy transport barrier, which effectively enhances hole extraction. Meanwhile, the valance band edge of vapor based perovskite also shifts upward because of the interfacial energy-level tuning due to excess MAI/FAI at the top surface, which agrees with the previous report.[43] The energy level alignment between NH4Cl-perovskite and SnO_2 also matches better. However, for the other two coated perovskite films the conduction band edge is below the conduction band edge of SnO_2 which shows an electron transfer barrier. This matched energy level alignment indicates better electron and hole transfer in the Perovskite/ETL and Perovskite/HTL interface.
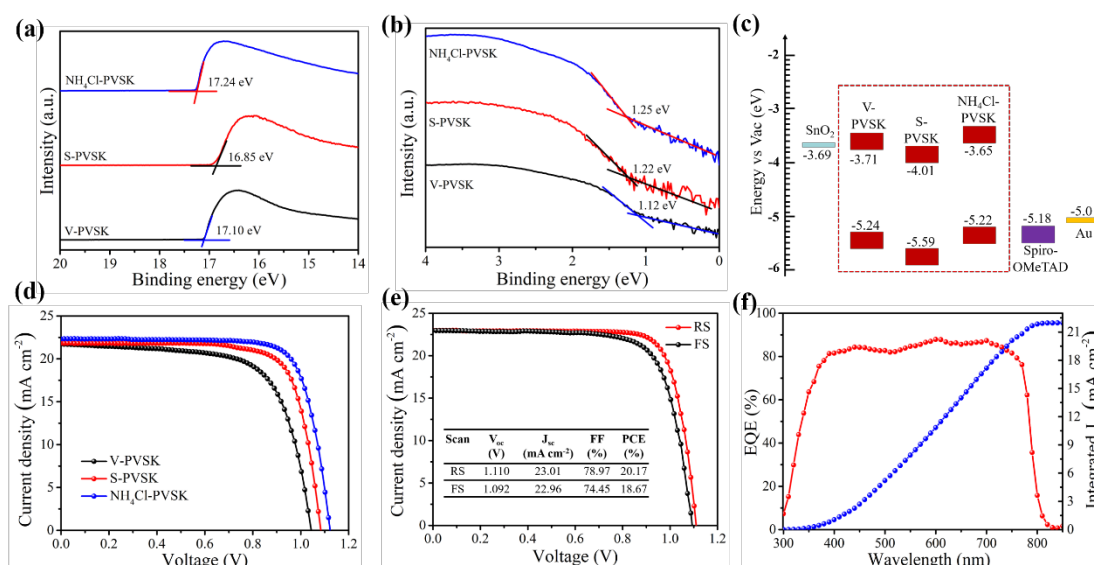
Figure 3. a) Secondary electron onset and b) valence features of the UPS spectra of the V-PVSK film, the S-PVSK film, and the NH4Cl-PVSK film. c) Energy diagram of perovskites. Note that in this energy diagram all energy levels are plotted with respect to the vacuum level, which is set to be 0 eV. d) Representative current density-voltage (J-V) curves of the PSCs under AM 1.5 G illumination. e) The best J-V curves. f) External quantum efficiency spectrum (EQE).

## 2.2. Lab-scale perovskite solar cells

The lab-scale small area PSCs were fabricated on 1.5×1.5 cm^2 indium doped tin

oxide (ITO) coated glass substrates with a configuration of ITO/SnO$_2$/perovskite/spiro-OMeTAD/Au, where spiro-OMeTAD is 2,2',7,7'-Tetrakis[N,N-di(4-methoxyphenyl)amino]-9,9'-spirobifluorene (Figure S17, Supporting Information). Statistical analyses of solar cell parameters based on a batch of 25 devices are shown in Figure S18 and Table S4 (Supporting Information). The average PCEs of the devices are 14.15%, 16.84% and 18.85% for vapor-based, conventional solution processed and NH$_4$Cl-perovskite PSCs, respectively. The J-V curves corresponding to the champion devices are shown in Figure 3d. Low efficiency of vapor-based PSCs is ascribed to the unreacted PbI$_2$ impeding electron transport and large defects in the perovskite film. In contrast, the improvement of the performance of NH$_4$Cl-perovskite PSCs can be explained by the improved energy level alignment, complete perovskite phase conversion, large grain size and monolithic-character of perovskite crystals, which increase the light absorption, decrease the electronic trap density and promote the carrier transport. Furthermore, we performed the EQE measurements on the champion devices to analyze the light absorption and conversion characteristics. The low EQE of the conventional solution processed perovskite PSCs at the short wavelength region (Figure S19, Supporting Information) reveals the existence of large amounts of unreacted PbI$_2$ in the films, which impedes light absorption and carrier collection at the SnO$_2$/PVSK interface because of the wider bandgap of PbI$_2$ and exciton recombination centers in unreacted PbI$_2$.[44] In contrast, the enhanced EQE spectrum of the NH$_4$Cl-perovskite PSC suggests the full conversion and high crystallinity in the perovskite film, which significantly boost up the light harvesting properties and reduce the trap density at the interface. Similarly, the high EQE of the NH$_4$Cl-perovskite PSC at the long wavelength region indicates a smaller trap density at the surface of the perovskite film and fast carrier extraction at the perovskite/HTL interface,[45] which is ascribed to the high quality of the perovskite film and the smaller energy barrier between NH$_4$Cl-perovskite and the HTL layer. Besides, the lower surface potential can also accelerate carrier transport,[34, 46] which will be discussed later. Figure 3e displays the champion device achieved by NH$_4$Cl method with an impressive PCE of 20.17% for the reverse scan (RS) and 18.67% for the forward scan (FS), which is much higher than previous

NH$_4$Cl based PSCs (Table S5, Supporting Information). The corresponding EQE in Figure 3f shows an integrated current density of 22.0 mA cm^{-2}, which agrees well with the value from the J-V curve (difference < 4.5%). Additionally, a stabilized output PCE of 18.67% was achieved by operating the device at the initial maximum power point of 0.93 V (Figure S20, Supporting Information).
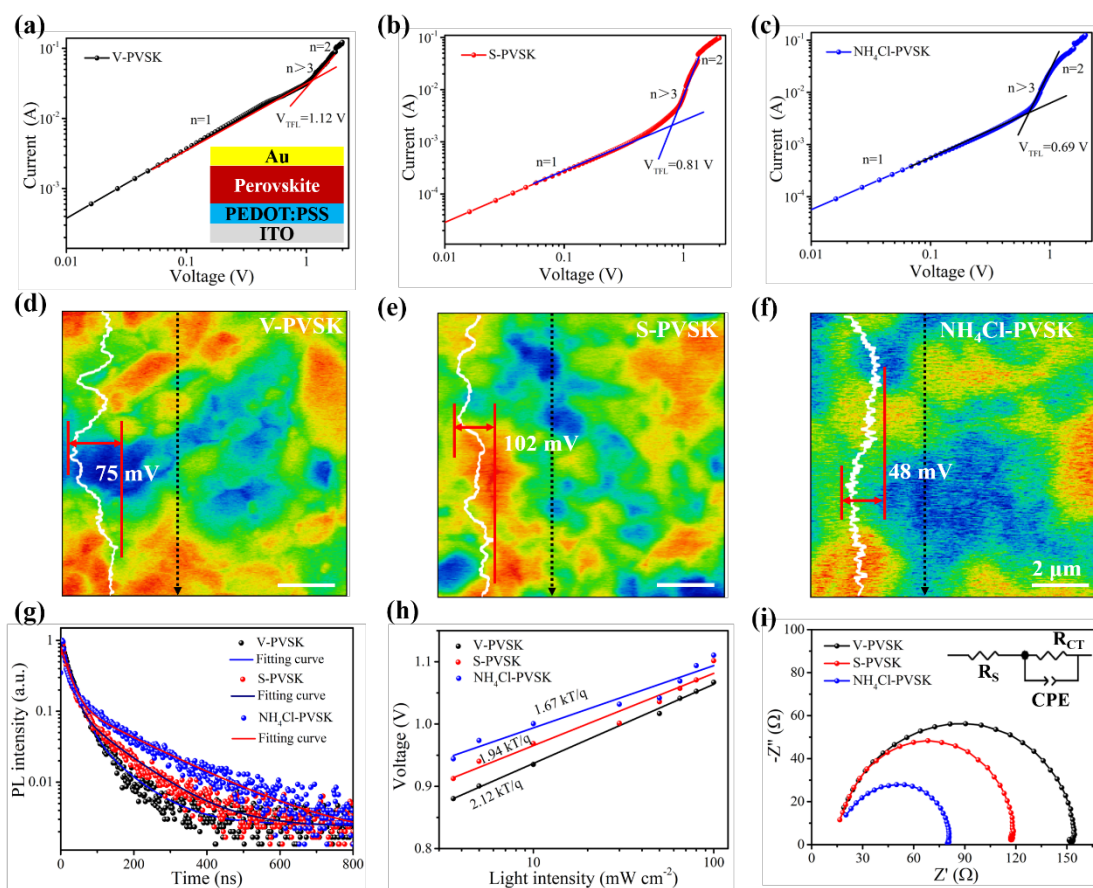
Figure 4. a)-c) Dark I-V characteristics of the devices with the ITO/PEDOT:PSS/perovskite/Au configuration of vapor based perovskite, conventional solution processed perovskite and NH$_4$Cl-perovskite. Kelvin probe force microscopy (KPFM) images of d) vapor-based perovskite film, e) conventional solution processed perovskite film, f) NH$_4$Cl-perovskite film on ITO glass. g) Time resolved photoluminescence (TRPL) decay curves of corresponding perovskite films on glass substrates. h) Open-circuit voltage (V$_{oc}$) as a function of light intensity curves. i) Nyquist plots and fitted circuit diagrams of PSCs.

2.3. Charge carrier transport behavior

The defect nature of the perovskite films were evaluated by characterization of space-charge limited current (SCLC) of hole-only (electron-only) devices with a perovskite film inserted between two hole (electron) transport layers, i.e., ITO/PEDOT:PSS/perovskite/Au (ITO/SnO$_2$/perovskite/PCBM/Ag), where PEDOT:PSS is poly (3, 4-ethylenedioxythiophene): poly (styrene sulfonate) and PCBM is phenyl-C61-butyric acid methyl ester.

$$V_{TFL} = \frac{N_\tau eL^2}{2\varepsilon\varepsilon_0} \qquad \text{(Eq. 4)}$$

where N_τ is the trap density. ε is defined as dielectric constants of perovskite and ε_0 is the vacuum permittivity.[47] L is the thickness of perovskite film, which can be determined by the cross-section images in Figure S21 (Supporting Information). e is the electric charge with a constant value of 1.602×10^{-19} C. Based on Eq. 4, we can find that the hole/electron trap density (**Figures 4**a-c and Figure S22, Supporting Information) significantly decreases from 6.27×10^{15} cm^{-3}/7.52×10^{15} cm^{-3} (vapor-based perovskite) to 1.22×10^{15} cm^{-3}/1.69×10^{15} cm^{-3} (conventional solution processed perovskite) for hole/electron only devices because of the formation of exciton recombination centers originated from the unreacted PbI$_2$ at the bottom layer.[44] In parallel, the reduced trap defects of NH$_4$Cl-perovskite (1.07×10^{15} cm^{-3} for hole only device and 1.22×10^{15} cm^{-3} for electron only device) indicate that the presence of intermediate phase can effectively improve the crystallinity and reduce the trap density of perovskite film. Additionally, it is worth noting that traps are predominantly located at the surface of perovskite and interface (perovskite/ETL and perovskite/HTL) and fewer defects in the bulk film, because of the loss of cations (MAI/FAI) and undercoordinated lead during the spin-coating and post-annealing.[40, 48-50] Therefore, high crystallinity and thick films can reduce the trap density.[51] To further understand the carrier transport behavior and evaluate the quality of perovskite films, we performed the surface potential measurement on the perovskite films using Kelvin probe force microscopy (KPFM). First, we investigated the surface morphology of the perovskite films. As presented in Figure S23 (Supporting Information), the NH$_4$Cl-perovskite film contains larger size grains and has a lower roughness (32.15 nm) compared with the

vapor deposition method (46.88 nm) and conventional solution processed (49.83 nm) perovskite films, which suggest that the NH_4Cl modification improved uniformity and compactness of the perovskite films. The corresponding topography and contact potential difference (CPD) mapping of the perovskite films (Figure S24, Supporting Information) also show a very low average surface potential difference of 9.8 mV for the NH_4Cl-perovskite film.[52] It is worth noting that the surface potential fluctuations of NH_4Cl- perovskite are much smaller than the other two samples, and the corresponding surface potential fluctuations difference along the vertical direction in Figures 4d-4f and Figure S25 (Supporting Information) is as low as 48 mV, which is much lower than vapor-based and conventional solution processed perovskite films, suggesting lack of significant band bending and surface defects in the NH_4Cl-perovskite films.[52-53] This low surface potential is ascribed to the flat surface in the film, which indicates a lower stress concentration at GBs. The transformation from PbI_2 to perovskite that leads to volume expansion as discussed before[24-25] induces an uneven growth of perovskite grains. In addition, the mismatched coefficients of thermal expansion (CTE) between the substrate ($2.6-10$ μK^{-1}) and perovskite film ($50-160$ μK^{-1}) during annealing at high temperature (150 °C) will also cause stress in the films when the samples cool down to the room temperature.[54-55] The above processes result in a high concentration of stress at GBs, which leads to a high surface potential between grains and GBs in the films.[34] The presence of the intermediate phase can facilitate the crystal rearrangement and slow down the nucleation rate (Figure 1b), which helps achieve uniform grain sizes and a lower stress concentration in the final films.[56] Besides, steady-state photoluminescent (PL) and time-resolved photoluminescence (TRPL) measurements were performed ~~with a 400 nm pulsed laser~~ to evaluate charge recombination and the quality of perovskite films. The PL intensity of NH_4Cl-PVSK is much higher than other two samples (Figure S26, Supporting Information) indicating the suppressed nonradiative recombination of the perovskite films after incorporation of NH_4Cl. In addition, a bi-exponential function is used to fit the curves as follows:[34, 56]

$$\tau_{ave} = \frac{A_1\tau_1^2 + A_2\tau_2^2}{A_1\tau_1 + A_2\tau_2} \quad \text{(Eq. 5)}$$

where A_1 and A_2 are the amplitudes, and the fast decay component of τ_1 and the slow decay component of τ_2 represent the non-radiative recombination and radiative recombination, respectively.[34, 40] The average carrier lifetimes (τ_{ave}) for vapor deposition, conventional solution and NH_4Cl-perovskite films in Figure 4g are 43.8 ns, 64.6 ns and 135.4 ns, respectively. The longer PL lifetime of NH_4Cl-perovskite is ascribed to its high crystal quality with less defects.[57] Instead, the shorter carrier lifetimes in vapor-based and conventional solution processed perovskite films highlight the influence of poor surface morphology and high surface potential voltage, because the unreacted PbI_2 and uneven grain size result in large trap density defects in the films. The decrease of A_1 (Table S6, Supporting Information) and increase of long lifetime (τ_2) component imply that less trap density and bulk carrier recombination in the case of NH_4Cl modified perovskite film in comparison of vapor-based and conventional solution perovskite films.[40, 58]

Furthermore, light-intensity-dependent V_{oc} of PSCs was also investigated under different illumination intensities (Figure 4i). The open-circuit voltage of the devices shows a monotonic increase as the light intensity increases. The deviation of the slope can be used to analyze the charge recombination behavior in the devices.[33, 59-60] For example, n equal to 1 indicates that charge recombination is dominated by free electrons and holes in the active layer. In contrast, if the n value reaches 2, trap-assisted Shockley–Read–Hall (SRH) recombination in the devices is dominant.[60] The n value can be extracted by fitting the curves following the equation:[60]

$$n = kT/q \frac{dV_{oc}}{d\ln(i)} \quad \text{(Eq. 6)}$$

where k is defined as the Boltzmann constant, T is the absolute temperature, q denotes the elementary charge, n and i are the ideality factor and light intensity, respectively.[59] The corresponding n values are 1.67, 1.91 and 2.02 for NH_4Cl-perovskite, conventional solution processed perovskite and vapor-based PSCs, respectively. The reduced slope indicates less trap-density in the NH_4Cl-perovskite film compared to other samples, which results in higher performance in devices. In addition, the electrochemical

impedance spectroscopy (EIS) tests were also carried out to further understand the charge carrier recombination under light illumination. The Nyquist plots of PSCs with different methods were performed at an applied bias of 1.0 V close to the V_{oc} under AM 1.5 illumination with a frequency ranging from 1 MHz to 100 Hz. By fitting the equivalent circuit (EC) diagram shown in Figure 4i, it is found that the semicircle can be defined as charge transport resistance (R_{ct}).[61] The corresponding sheet resistance (R_s) values of all the devices are very close because of the same configuration in PSCs.[62] The smallest R_{ct} of NH_4Cl-perovskite (65.68 Ω) solar cell indicates the fastest carrier transport, which is ascribed to the high crystallinity and low surface potential fluctuations in the NH_4Cl-perovskite film. These advantages can help form a smaller energy barrier and fewer traps in the film and at the interface. In comparison, vapor-based perovskite (141.7 Ω) and conventional solution processed perovskite (103.5 Ω) devices have higher charge transport resistances (Table S7, Supporting Information).
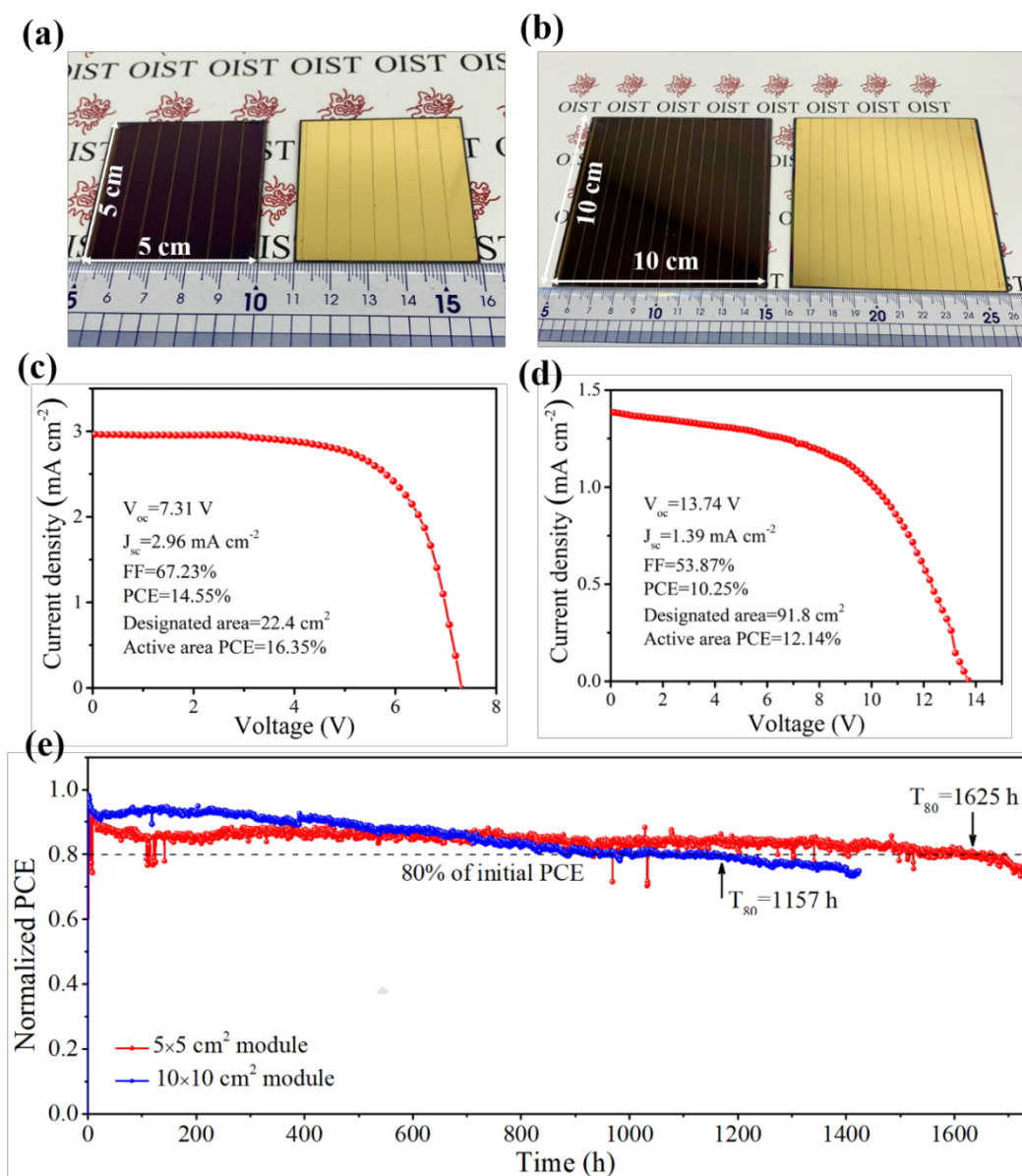
Figure 5. Photographs of a) 5×5 cm^2 and b) 10×10 cm^2 PSMs. J-V curves of c) 5×5 cm^2 and d) 10×10 cm^2 PSMs. e) Operational stability of PSMs under a steady applied voltage, which corresponds to the initial maximum power point voltage from the J-V curves.

2.4. Up-scalable perovskite solar modules and operational stability

Up-scalable fabrication protocols of PSCs are also important aspect to realize their industrialization. Based on the same device configuration developed for lab-scale PSCs, we upscaled the process and developed a 5×5 cm^2 PSM with a designated area of 22.4 cm^2. As seen in **Figure 5**a, the PSM consists of 7 sub-cells in series on a 5×5 cm^2 ITO

substrate (Figure S27, Supporting Information). It is found that the perovskite layer is uniform across the entire 5 cm × 5 cm^2 substrate. The thickness of the perovskite layer is approximately 1.1 µm (Figure S28, Supporting Information). Statistical analyses of performance based on 20 PSMs (substrate size = 5×5 cm^2) for the conventional solution process and NH$_4$Cl method are shown in Figures S29, S30 and Tables S8, S9 (Supporting Information). The PCEs of PSMs fabricated by NH$_4$Cl method ranges from 11% to 14% with an average performance of 13.23 ± 0.63%. The champion PCE of all fabricated devices achieves 14.55% with a V$_{oc}$ of 7.31 V, a J$_{sc}$ of 2.96 mA cm^{-2} and a FF of 67.23% for the reverse scan and the PCE of 12.81% for the forward scan (Figure S31a, Supporting Information) with a designated area of 22.4 cm^2. The corresponding active area efficiency of the champion PSM is up to 16.35% with a GFF of 89% (Figure S31b, Supporting Information). In contrast, the efficiency of PSMs prepared by the conventional solution process ranges from 7% to 13% with an average PCE of 10.05 ± 1.58%. The resultant champion PCE is only 13.06% under reverse scan (Figure S32a, Supporting Information). The corresponding active area efficiency is 14.84% with a GFF of 88% (Figure S32b, Supporting Information). Moreover, operational stability is also an important parameter to evaluate the performance of PSMs. First, we evaluated the operational stability of our PSMs without encapsulation under continuous AM 1.5G light illumination at a given bias of the initial maximum power point (MPP) in ambient environment (RH~55%, 25 ºC). As seen in Figure S33 (Supporting information), the operational stability of NH$_4$Cl-PVSK perovskite solar module was the best, maintaining 80.3% of the initial PCE after 300 min. S-PVSK based solar module retained 74.9% of its initial PCE at 100 min. V-PVSK based solar module showed a significant decrease in PCE (67.8% of its initial efficiency at 100 min). Moreover, we study the stability of NH$_4$Cl-PVSK solar module with parylene encapsulation under continuous AM 1.5G light illumination at a given bias of the initial maximum power point (MPP) in dry N$_2$ flow environment. The T$_{80}$ lifetime of PSMs is up to 1625 h, which showed a better operational stability than the previous reports as seen in Table S1 (Supporting Information). The encapsulated 5×5 cm^2 PSM can power a mini-fan working well in outdoor conditions (Figure S34 and Supplementary Video, Supporting Information).

To further verify the upscalability of our method, we fabricated PSMs with 14 sub-cells in series on a 10×10 cm^2 ITO substrate (Figure S35, Supporting Information) using the similar method (Figure 5b). Note that PSMs with an area greater than 5×5 cm^2 are rarely reported in previous works. Additionally, scaling up the solar modules from 5×5 cm^2 to 10×10 cm^2, the increased series resistance from ITO substrates and the ITO/SnO$_2$/Au interconnections (between the top electrode of one sub-cell and the ITO bottom electrode of the next adjacent sub-cell) and reduced shunt resistance from extra seven times laser scribing for P2 and mechanical scribing for P3 also have significant effects on the performance of modules.[5] Statistical analyses of performance data based on 10 PSMs (substrate size = 10×10 cm^2) are presented in Figure S36 and Table S10 (Supporting Information). The PCEs of PSMs range from 6% to 10% with an average performance of $8.63 \pm 1.06\%$. As we can see in Figure 5d, the highest PCE of 10.25% is achieved with a V_{oc} of 13.74 V, a J_{sc} of 1.39 mA cm^{-2} and an FF of 53.67% with a designated area of 91.86 cm^2 for 10×10 cm^2 PSMs. The corresponding GFF of PSM is 84.4% (Figure S37, Supporting Information), which indicates that the active area PCE is up to 12.14%. The 10×10 cm^2 PSMs also show low hysteresis (Figure S37, Supporting Information). Importantly, we conducted the operational stability of 10×10 cm^2 PSM in the same environment as 5×5 cm^2 PSM before by recording the 10×10 cm^2 PSM power output under a steady applied voltage, which corresponds to the initial maximum power point voltage from J-V curve. It is found that the 10×10 cm^2 PSMs exhibited an excellent operational stability and kept 90% of the initial PCE for more than 450 h. The T_{80} lifetime of 10×10 cm^2 PSM in Figure 5e is 1157 h, which is the first report on the operational stability of 10×10 cm^2 PSMs. Furthermore, to evaluate the performance of a solar module, a PSM-powered toy car was made using 10×10 cm^2 PSM (Figure S38, Supporting Information). The toy car could start under the continuous light illumination as seen in Supplementary Video. When we moved the car outside the laboratory, we found that the PSM-powered toy car could run on the road outdoor (Supplementary Video).

The good operational stability is a result of the following three factors. First of all, our PSMs feature a thick perovskite layer (over one-micrometer), the top layer of which

can serve as a protection layer against oxygen and moisture ingress slowing down the degradation rate of the inner parts of the perovskite film.[12, 16, 63] Secondly, the partial substitution of FA^+ cations with MA^+ and/or Cs^+ to construct mixed cation perovskites can alleviate the phase transition and improve the stability of the cubic phase of perovskites.[64-65] Thirdly, the large grain size of the perovskite film in our PSMs helps increase stability. Perovskite decomposition starts from the GBs because of the existence of stress and favorable ion migration at the GBs.[34, 66] Large grain size (over one-micrometer) and the small number of GBs in NH_4Cl-perovskite films reduce the degradation kinetics in comparison to the ones fabricated from the conventional methods that often leads to small grain size and high concentration of GBs. The low surface potential difference in the NH_4Cl-perovskite films also suggests less stress between perovskite grains during fabrication, which can alleviate the decomposition starting at GBs.[34, 67] Last but not least, high crystallinity of perovskite films leads to less defects in the films, which allows fast carrier extraction and reduced charge trapping at the GBs under light illumination. The large amounts of charge trapping at the GBs or films induced by light soaking in the moisture environment/heat conditions can lead to the irreversible degradation of perovskite films.[56, 68]

3. Conclusions

In conclusion, we report a perovskite formation strategy to deposit a one-micrometer-thick perovskite layer by introducing NH_4Cl as an additive for up-scalable fabrication of PSMs. The incorporation of NH_4Cl can significantly enhance the solubility of PbI_2 in DMF and form the intermediate phases of $x[NH_4^+] \cdot [PbI_2Cl_x]^{x-}$ and $HPbI_{3-x}Cl_x$. The presence of the intermediate phases can effectively slow down the nucleation rate and increase the crystallinity of perovskite films, leading to uniform perovskite films. The NH_4Cl-incorporated perovskite films achieved a high PCE of 20.17% in the lab-scale small size PSC (0.09 cm^2), 14.55% (active area PCE 16.35%) in the 5×5 cm^2 PSM (22.4 cm^2) and 10.25% (active area PCE 12.14%) in the 10×10 cm^2 PSM (91.8 cm^2). Furthermore, this strategy also shows a great potential in improving the stability of devices. The operational stability of PSMs under a steady voltage output showed the

T_{80} lifetime of 5×5 cm^2 and 10×10 cm^2 PSMs to exceed 1600 h and 1100 h, respectively, under continuous light illumination.

Supporting Information

Supporting Information and Supplementary Video are available from the Wiley Online Library or from the author.

Conflict of Interest

The authors declare no conflict of interest.

References

[1]   N. J. Jeon, H. Na, E. H. Jung, T.-Y. Yang, Y. G. Lee, G. Kim, H.-W. Shin, S. Il Seok, J. Lee, J. Seo, *Nat. Energy* **2018**, *3*, 682.

[2]   Z. Liu, L. Qiu, L. K. Ono, S. He, Z. Hu, M. Jiang, G. Tong, Z. Wu, Y. Jiang, D.-Y. Son, Y. Dang, S. Kazaoui, Y. B. Qi, *Nat. Energy* **2020**, *5*, 596.

[3]   Best research-cell efficiencies. https://www.nrel.gov/pv/assets/pdfs/best-research-cell-efficiencies.20200919.pdf.

[4]   J. Werner, C. C. Boyd, T. Moot, E. J. Wolf, R. M. France, S. A. Johnson, M. F. A. M. van Hest, J. M. Luther, K. Zhu, J. J. Berry, M. D. McGehee, *Energy Environ. Sci.* **2020**, *13*, 3393.

[5]   L. Qiu, S. He, L. K. Ono, S. Liu, Y. B. Qi, *ACS Energy Lett.* **2019**, *4*, 2147.

[6]   Z. Li, T. R. Klein, D. H. Kim, M. Yang, J. J. Berry, M. F. A. M. van Hest, K. Zhu, *Nat. Rev. Mater.* **2018**, *3*, 18017.

[7]   D. H. Kim, J. B. Whitaker, Z. Li, M. F. A. M. van Hest, K. Zhu, *Joule* **2018**, *2*, 1437.

[8]   A. Ren, H. Lai, X. Hao, Z. Tang, H. Xu, B. M. F. Yu Jeco, K. Watanabe, L. Wu, J. Zhang, M. Sugiyama, J. Wu, D. Zhao, *Joule* **2020**, *4*, 1263.

[9]   L. Qiu, S. He, Y. Jiang, D.-Y. Son, L. K. Ono, Z. Liu, T. Kim, T. Bouloumis, S. Kazaoui, Y. B. Qi, *J. Mater. Chem. A* **2019**, *7*, 6920.

[10]   Y. Jiang, M. Remeika, Z. Hu, E. J. Juarez-Perez, L. Qiu, Z. Liu, T. Kim, L. K. Ono, D. Y. Son, Z. Hawash, M. R. Leyden, Z. Wu, L. Meng, J. Hu, Y. B. Qi, *Adv. Energy Mater.* **2019**, *9*, 1803047.

[11]   J. Hu, C. Wang, S. Qiu, Y. Zhao, E. Gu, L. Zeng, Y. Yang, C. Li, X. Liu, K. Forberich, C. J. Brabec, M. K. Nazeeruddin, Y. Mai, F. Guo, *Adv. Energy Mater.* **2020**, *10*, 2000173.

[12]   Z. Liu, L. Qiu, E. J. Juarez-Perez, Z. Hawash, T. Kim, Y. Jiang, Z. Wu, S. R. Raga, L. K. Ono, S. F. Liu, Y. B. Qi, *Nat. Commun.* **2018**, *9*, 3880.

[13]   G. E. E. Samuel D. Stranks, Giulia Grancini, Christopher Menelaou,, T. L. Marcelo J. P. Alcocer, Laura M. Herz, Annamaria Petrozza, Henry J. Snaith, *Science* **2013**, *342*, 341.

[14]   Z. Chen, B. Turedi, A. Y. Alsalloum, C. Yang, X. Zheng, I. Gereige, A. AlSaggaf, O. F. Mohammed, O. M. Bakr, *ACS Energy Lett.* **2019**, *4*, 1258.

[15]   H. Eggers, F. Schackmar, T. Abzieher, Q. Sun, U. Lemmer, Y. Vaynzof, B. S. Richards, G. Hernandez-Sosa, U. W. Paetzold, *Adv. Energy Mater.* **2019**, *10*, 1903184.

[16]   J. Chen, L. Zuo, Y. Zhang, X. Lian, W. Fu, J. Yan, J. Li, G. Wu, C.-Z. Li, H. Chen, *Adv. Energy Mater.* **2018**, *8*, 1800438.

[17]   S. Masi, F. Aiello, A. Listorti, F. Balzano, D. Altamura, C. Giannini, R. Caliandro, G. Uccello-Barretta, A. Rizzo, S. Colella, *Chem. Sci.*, **2018**, *9*, 3200.

[18]   J.-W. Lee, H.-S. Kim, N.-G. Park, *Acc. Chem. Res.* **2016**, *49*, 311.

[19]   C. Fei, B. Li, R. Zhang, H. Fu, J. Tian, G. Cao, *Adv. Energy Mater.* **2016**, *7*, 1602017.

[20]   H. Si, Q. Liao, Z. Kang, Y. Ou, J. Meng, Y. Liu, Z. Zhang, Y. Zhang, *Adv. Funct. Mater.* **2017**, *27*, 1701804.

[21]   Q. Li, Y. Zhao, R. Fu, W. Zhou, Y. Zhao, X. Liu, D. Yu, Q. Zhao, *Adv. Mater.* **2018**, *30*, 1803095.

[22]   J.-Y. Seo, T. Matsui, J. Luo, J.-P. Correa-Baena, F. Giordano, M. Saliba, K. Schenk, A. Ummadisingu, K. Domanski, M. Hadadian, A. Hagfeldt, S. M. Zakeeruddin, U. Steiner, M. Grätzel, A. Abate, *Adv. Energy Mater.* **2016**, *6*, 1600767.

[23]   F. Wang, H. Yu, H. Xu, N. Zhao, *Adv. Funct. Mater.* **2015**, *25*, 1120.

[24]   M. R. Leyden, L. K. Ono, S. R. Raga, Y. Kato, S. Wang, Y. B. Qi, *J. Mater. Chem. A* **2014**, *2*, 18742.

[25]   Q. Chen, H. Zhou, Z. Hong, S. Luo, H. S. Duan, H. H. Wang, Y. Liu, G. Li, Y. Yang, *J. Am. Chem. Soc.* **2014**, *136*, 622.

[26]   Y. Zhao, K. Zhu, *Chem. Soc. Rev.* **2016**, *45*, 655.

[27]   J. Wang, S. Luo, Y. Lin, Y. Chen, Y. Deng, Z. Li, K. Meng, G. Chen, T. Huang, S. Xiao, H. Huang, C. Zhou, L. Ding, J. He, J. Huang, Y. Yuan, *Nat. Commun.* **2020**, *11*, 582.

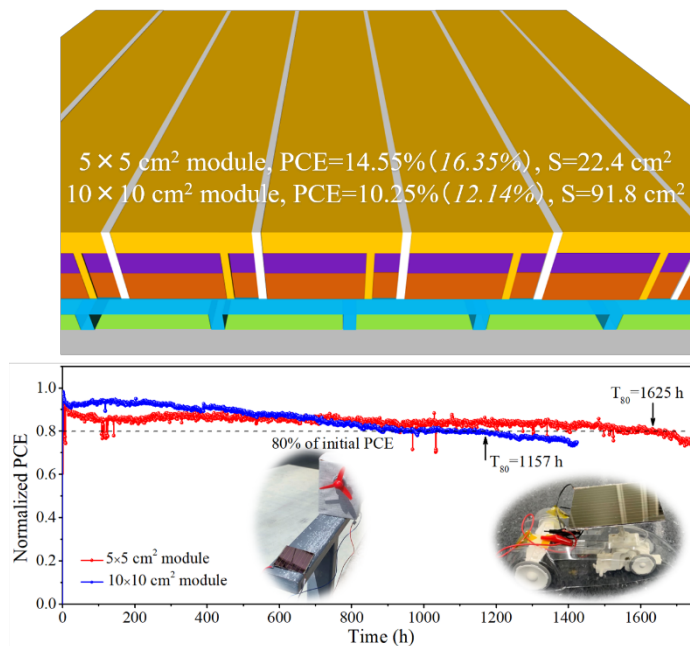[28]   J. Li, R. Munir, Y. Fan, T. Niu, Y. Liu, Y. Zhong, Z. Yang, Y. Tian, B. Liu, J. Sun,

D.-M. Smilgies, S. Thoroddsen, A. Amassian, K. Zhao, S. F. Liu, *Joule* **2018**, *2*, 1313.

[29] X. Dai, Y. Deng, C. H. Van Brackle, S. Chen, P. N. Rudd, X. Xiao, Y. Lin, B. Chen, J. Huang, *Adv. Energy Mater.* **2019**, *10*, 1903108.

[30] G. Tong, X. Lan, Z. Song, G. Li, H. Li, L. Yu, J. Xu, Y. Jiang, Y. Sheng, Y. Shi, K. Chen, *Mater. Today Energy* **2017**, *5*, 173.

[31] Y. He, W. Wang, L. Qi, *ACS Appl. Mater. Interfaces* **2018**, *10*, 38985.

[32] S. Pang, Y. Zhou, Z. Wang, M. Yang, A. R. Krause, Z. Zhou, K. Zhu, N. P. Padture, G. Cui, *J. Am. Chem. Soc.* **2016**, *138*, 750.

[33] Z. Liu, K. Deng, J. Hu, L. Li, *Angew.Chem. Int. Ed.* **2019**, *58*, 11497.

[34] G. Tong, T. Chen, H. Li, L. Qiu, Z. Liu, Y. Dang, W. Song, L. K.Ono, Y. Jiang, Y. B. Qi, *Nano Energy* **2019**, *65*, 104015.

[35] T. Zhang, M. Yang, Y. Zhao, K. Zhu, *Nano Lett.* **2015**, *15*, 3959.

[36] G. Tong, Z. Song, C. Li, Y. Zhao, L. Yu, J. Xu, Y. Jiang, Y. Sheng, Y. Shi, K. Chen, *RSC Adv.* **2017**, *7*, 19457.

[37] H. Zhang, J. Mao, H. He, D. Zhang, H. L. Zhu, F. Xie, K. S. Wong, M. Grätzel, W. C. H. Choy, *Adv. Energy Mater.* **2015**, *5*, 1501354.

[38] G. Grancini, C. Roldan-Carmona, I. Zimmermann, E. Mosconi, X. Lee, D. Martineau, S. Narbey, F. Oswald, F. De Angelis, M. Graetzel, M. K. Nazeeruddin, *Nat. Commun.* **2017**, *8*, 15684.

[39] T. Chen, G. Tong, E. Xu, H. Li, P. Li, Z. Zhu, J. Tang, Y. B. Qi, Y. Jiang, *J. Mater. Chem. A* **2019**, *7*, 20597.

[40] Z. Wu, M. Jiang, Z. Liu, A. Jamshaid, L. K. Ono, Y. B. Qi, *Adv. Energy Mater.* **2020**, *10*, 1903696.

[41] S. Wang, Z. Li, Y. Zhang, X. Liu, J. Han, X. Li, Z. Liu, S. F. Liu, W. C. H. Choy, *Adv. Funct. Mater.* **2019**, *29*, 1900417.

[42] J. Emara, T. Schnier, N. Pourdavoud, T. Riedl, K. Meerholz, S. Olthof, *Adv. Mater.* **2016**, *28*, 553.

[43] Z. Hawash, S. R. Raga, D.-Y. Son, L. K. Ono, N. G. Park, Y. B. Qi, *J. Phys. Chem. Lett.* **2017**, *8*, 3947.

[44] X. Duan, X. Li, L. Tan, Z. Huang, J. Yang, G. Liu, Z. Lin, Y. Chen, *Adv. Mater.* **2020**, *32*, 2000617.

[45] T. Bu, L. Wu, X. Liu, X. Yang, P. Zhou, X. Yu, T. Qin, J. Shi, S. Wang, S. Li, Z. Ku, Y. Peng, F. Huang, Q. Meng, Y.-B. Cheng, J. Zhong, *Adv. Energy Mater.* **2017**, *7*, 1700576.

[46] A. Dymshits, A. Henning, G. Segev, Y. Rosenwaks, L. Etgar, *Sci. Rep.* **2015**, *5*, 8704.

[47] D.-Y. Son, S. G. Kim, J. Y. Seo, S. H. Lee, H. Shin, D. Lee, N. G. Park, *J. Am. Chem. Soc.* **2018**, *140*, 1358.

[48] Z. Chen, Q. Dong, Y. Liu, C. Bao, Y. Fang, Y. Lin, S. Tang, Q. Wang, X. Xiao, Y. Bai, Y. Deng, J. Huang, *Nat. Commun.* **2017**, *8*, 1890.

[49] L. K. Ono, S. Liu, Y. B. Qi, *Angew.Chem. Int. Ed.* **2020**, *59*, 6676.

[50] D. Meggiolaro, E. Mosconi, F. De Angelis, *ACS Energy Lett.* **2019**, *4*, 779.

[51] Z. Xu, Z. Liu, Y. Huang, G. Zheng, Q. Chen, H. Zhou, *J. Mater. Chem. C* **2017**, *5*, 5810.

[52] Y. Zhou, L. Wang, S. Chen, S. Qin, X. Liu, J. Chen, D.-J. Xue, M. Luo, Y. Cao, Y. Cheng, E. H. Sargent, J. Tang, *Nat. Photonics* **2015**, *9*, 409.

[53] J. S. Yun, A. Ho-Baillie, S. Huang, S. H. Woo, Y. Heo, J. Seidel, F. Huang, Y. B. Cheng, M. A. Green, *J. Phys. Chem. Lett.* **2015**, *6*, 875.

[54] K. A. Bush, N. Rolston, A. Gold-Parker, S. Manzoor, J. Hausele, Z. J. Yu, J. A. Raiford, R. Cheacharoen, Z. C. Holman, M. F. Toney, R. H. Dauskardt, M. D. McGehee, *ACS Energy Lett.* **2018**, *3*, 1225.

[55] J. Zhao, Y. Deng, H. Wei, X. Zheng, Z. Yu, Y. Shao, J. E. Shield, J. Huang, *Sci. Adv.* **2017**, *3*, eaao5616.

[56] G. Tong, M. Jiang, D. Y. Son, L. K. Ono, Y. B. Qi, *Adv. Funct. Mater.* **2020**, *30*, 2002526.

[57] F. Bai, J. Zhang, Y. Yuan, H. Liu, X. Li, C. C. Chueh, H. Yan, Z. Zhu, A. K. Jen, *Adv. Mater.* **2019**, *31*, 1904735.

[58] S. Tan, N. Zhou, Y. Chen, L. Li, G. Liu, P. Liu, C. Zhu, J. Lu, W. Sun, Q. Chen, H. Zhou, *Adv. Energy Mater.* **2018**, *9*, 1803024.

[59] T. Bu, J. Li, F. Zheng, W. Chen, X. Wen, Z. Ku, Y. Peng, J. Zhong, Y. B. Cheng, F. Huang, *Nat. Commun.* **2018**, *9*, 4609.

[60] H. Zhang, X. Ren, X. Chen, J. Mao, J. Cheng, Y. Zhao, Y. Liu, J. Milic, W.-J. Yin, M. Grätzel, W. C. H. Choy, *Energy Environ. Sci.* **2018**, *11*, 2253.

[61] C. Ma, D. Shen, T. W. Ng, M. F. Lo, C. S. Lee, *Adv. Mater.* **2018**, *30*, 1800710.

[62] B. Parida, J. Ryu, S. Yoon, S. Lee, Y. Seo, J. S. Cho, D.-W. Kang, *J. Mater. Chem. A* **2019**, *7*, 18488.

[63] G. Tong, M. Jiang, D.-Y. Son, L. Qiu, Z. Liu, L. K. Ono, Y. B. Qi, *ACS Appl. Mater. Interfaces* **2020**, *12*, 14185.

[64] H. E. Sánchez-Godoy, E. A. Erazo, A. F. Gualdrón-Reyes, A. H. Khan, S. Agouram, E. M. Barea, R. A. Rodriguez, I. Zarazúa, P. Ortiz, M. T. Cortés, V. Muñoz-Sanjosé, I. Moreels, S. Masi, I. Mora-Seró, *Adv. Energy Mater.* **2020**, *10*, 2002422.

[65] N. Li, Y. Luo, Z. Chen, X. Niu, X. Zhang, J. Lu, R. Kumar, J. Jiang, H. Liu, X. Guo, B. Lai, G. Brocks, Q. Chen, S. Tao, D. P. Fenning, H. Zhou, *Joule*, **2020**, *4*, 1743.

[66] Y. Yuan, J. Huang, *Acc. Chem. Res.* **2016**, *49*, 286.

[67] L. Shi, M. P. Bucknall, T. L. Young, M. Zhang, L. Hu, J. Bing, D. S. Lee, J. Kim, T. Wu, N. Takamure, D. R. McKenzie, S. Huang, M. A. Green, A. W. Y. Ho-Baillie, *Science* **2020**, *368*, eaba2412.

[68] N. Ahn, K. Kwak, M. S. Jang, H. Yoon, B. Y. Lee, J.-K. Lee, P. V. Pikhitsa, J. Byun, M. Choi, *Nat. Commun.* **2016**, *7*, 13422.

1 **TOC**

2

5×5 cm^2 module, PCE=14.55%(16.35%), S=22.4 cm^2
10×10 cm^2 module, PCE=10.25%(12.14%), S=91.8 cm^2

4 High performance perovskite solar modules (PSMs) were fabricated by introducing

5 NH$_4$Cl to induce the formation of the intermediate phases. The PSMs showed a long-

6 term operational stability with a T$_{80}$ lifetime under continuous light illumination

7 exceeding 1600 h for 5×5 cm^2 solar module and 1100 h for 10×10 cm^2 solar module,

8 respectively.

9
10
11
12
13